Quadrupole moments in chiral material $DyFe_3(BO_3)_4$ observed by resonant x-ray diffraction

Hiroshi Nakajima,[1,2] Tomoyasu Usui,[1] Yves Joly,[3,4] Motohiro Suzuki,[5]
Yusuke Wakabayashi,[1] Tsuyoshi Kimura,[1] and Yoshikazu Tanaka[6,*]

[1] *Division of Materials Physics, Graduate School of Engineering Science, Osaka University, Toyonaka, Osaka 560-8531, Japan*

[2] *Department of Materials Science, Graduate School of Engineering, Osaka Prefecture University, Sakai, Osaka 599-8531*

[3] *Université Grenoble Alpes, Institut NEEL, F-38042 Grenoble, France*

[4] *CNRS, Institut NEEL, F-38042 Grenoble, France*

[5] *Japan Synchrotron Radiation Research Institute (JASRI), Sayo, Hyogo 679-5198, Japan*

[6] *RIKEN SPring-8 Center, Sayo, Hyogo 679-5148, Japan*

(Dated: September 29, 2015)

arXiv:1509.08298v1 [cond-mat.mtrl-sci] 28 Sep 2015

Abstract

By means of circularly polarized x-ray beam at Dy L_3 and Fe K absorption edges, the chiral structure of the electric quadrupole was investigated for a single crystal of $DyFe_3(BO_3)_4$ in which both Dy and Fe ions are arranged in spiral manners. The integrated intensity of the resonant x-ray diffraction of space-group forbidden reflections 004 and 005 is interpreted within the electric dipole transitions from Dy $2p_{\frac{3}{2}}$ to $5d$ and Fe $1s$ to $4p$, respectively. We have confirmed that the handedness of the crystal observed at Dy L_3 and Fe K edges is consistent with that observed at Dy M_5 edge in the previous study. By analyzing the azimuth scans of the diffracted intensity, the electronic quadrupole moments of Dy $5d$ and Fe $4p$ are derived. The temperature profiles of the integrated intensity of 004 at the Dy L_3 and the Fe K edges are similar to those of Dy-O and Fe-O bond lengths, while that at the Dy M_5 edge does not. The results indicate that the helix chiral orientations of quadrupole moments due to Dy $5d$ and Fe $4p$ electrons are more strongly affected by the crystal fields than Dy $4f$.

PACS numbers: 61.05.cp, 75.25.Dk

I. INTRODUCTION

Chirality is one of the most important concepts over a wide range of science, including particle physics, cosmology, biology, pharmacy, condensed matter physics, and industry, etc.[1,2] The key issue of chirality, or handedness, is the break of symmetry that plays a crucial role in a variety of the fields. In condensed matter physics, the break of symmetry often gives an excellent arena to manipulate the physical properties. One prominent example is found in the magnetoelectric multiferroic materials, where the ferroelectricity appears as a result of the phase transition inducing such a magnetic order that breaks the inversion symmetry.[3,4] Many of them have a cycloidal or a screw spin structure, of which handedness determines the sign of the spontaneous electric polarization. In such a system, the multipole moments demonstrate the sign of handedness together with the atomic and spin structure. The electric multipole is represented by the density of the electron cloud at an ion which is expanded with the spherical tensor T_Q^K. Here K represents the rank of tensor, and Q, $-K \leq Q \leq K$, represents its projection. In principle, the electric multipole $\langle T_Q^K \rangle$ is visible with an x-ray beam because the electron has the large cross-section for the x-ray beam. In reality, however, observing a motif of the multipoles in crystal is not easy in x-ray diffraction. In the conventional x-ray diffraction, which is used to observe the crystal structure, the diffraction profile is mainly emerged from the core electrons of the consisting elements in the matter, where the contribution of the valence electrons is negligible. Whereas, when the system has the antiferroic type of the multipole order, where the symmetry of valence electrons breaks the crystal symmetry, the order is visible with the high intense x-ray beam from the synchrotron radiation source. For example, it has been found that the antiferroic quadrupole order in CeB_6 at low temperatures shows tiny superlattice reflections $\left(\frac{h}{2}, \frac{k}{2}, \frac{l}{2}\right)$, where h, k, and l are odd numbers.[5,6]

Since the discovery of linear dichroism[7] and forbidden reflections[8] at an absorption edge, resonant x-ray diffraction (RXD) has been developed to investigate a variety of ordered states, such as magnetic, charge, or orbital orders. The atomic picture of the resonance is well known: an incoming photon promotes a core electron to empty states, and it returns to the same core hole, emitting a second photon of the same energy as the incoming one. The scattering length at an absorption edge, which is sensitive to the polarization in the primary and secondary x rays, carries site-specific information on unoccupied valence states

on and around the resonant ion. This sensitivity provides another useful aspect of RXD as described below.

Circular dichroism in RXD has been found for low-quartz,[9,10] which has an enantiomorphic space-group pair, $P3_121$ (right-handed screw) and $P3_221$ (left-handed screw). In crystals having the space-group pair $P3_121$ and $P3_221$, reflections $00l$ ($l \neq 3n$, n =integer) are forbidden in non-resonant x-ray diffraction, but allowed in RXD for certain x-ray energies because of the sensitivity of the atomic scattering length to the x-ray polarization. By carefully examining the space-group forbidden reflections observed with circularly-polarized x rays, one can identify the absolute sign of the crystallographic helix chirality.[11,12] For the ferromagnetic or the ferroelectric states, we hardly know the state of the valence electrons by x-ray diffraction, because the symmetry of the magnetic order or the charge order is the same as the crystal symmetry. However, for the system having the screw-axis or the glide-plane, we can scrutinize the ordering state of the multipole moment, observing the space-group forbidden reflections,[13] even though the symmetry is the same as the crystal symmetry.

Recently we have successfully shown that RXD using circularly polarized x rays not only identifies the absolute sign of the crystallographic helix chirality, but also provides direct information on the multipole moments accompanied with the crystallographic helix chirality.[14] We have determined two components among five of the $4f$ quadrupole moment of Dy in $DyFe_3(BO_3)_4$ where the motif of the $4f$ quadrupole moment coincides with the crystallographic helix chirality. In the experiment, we have observed forbidden reflection 001 with circularly polarized soft x-ray beam at Dy M_5 absorption edge, where the x rays enhance the resonance from the $3d_{\frac{5}{2}}$ state to the vacant $4f$ state. Accordingly the signal observed in the diffraction gives the information of the $4f$ quadrupole moment of Dy ions.

In the present study, we demonstrate that circularly polarized hard x-ray beam at two absorption edges, Dy L_3 and Fe K, is also useful to determine the absolute sign of crystal chirality in $DyFe_3(BO_3)_4$ as the soft x-ray beam at Dy M_5 absorption edge. The resonance from Dy $2p_{\frac{3}{2}}$ to $5d$ at Dy L_3 absorption edge, and that from Fe $1s$ to $4p$ at Fe K absorption edge give the information of Dy $5d$ quadrupole moment and the Fe $4p$ quadrupole moment, respectively. We discuss the possibility of the birefringence phenomenon and the higher-order transition like $E1E2$ for the observed data. We also discuss the chirality in terms of the electric Dy $5d$ quadrupole moment and the Fe $4p$ quadrupole moment together with the

deformation of the crystal structure as a function of temperature.

We give a general background of resonant x-ray diffraction in Sec. II. We describe the crystal structure of $DyFe_3(BO_3)_4$ as well as the physical properties in Sec. III and the experimental geometry in Sec IV. In Sec. V, we show the experimental results of the resonant diffraction both at Dy L_3 and Fe K absorption edges: x-ray absorption spectra, azimuth angle scans, and the temperature dependence of the integrated intensity of forbidden reflection 004. In Sec. VI, we analyze the azimuth scan data and derive the Dy $5d$ quadrupole moment and the Fe $4p$ quadrupole moment with theoretical interpretations. In addition, we discuss the temperature dependence in terms of the deformation of DyO_6 trigonal prism and FeO_6 octahedron.

II. RESONANT X-RAY DIFFRACTION

The determination of the absolute structure of enantiomers, which have exactly the mirror image to each other, is not easy because they have the same chemical formula and atom to atom arrangements, and hence has been considered as an important challenge of crystallography. Among many methods applied for the determination so far, x-ray diffraction with dispersion corrections has played an important role for a long time.

The scattering length of x-rays for an atom can be written as

$$f = f_0 + f' + if'', \tag{1}$$

where f_0 is the energy-independent x-ray scattering length and corresponds to the Fourier transform of the electron density around the atom, f' and f'' are the real and the imaginary parts, respectively, of the dispersion correction. Note that the sign of f'', which is positive in the conventional x-ray diffraction, is negative in our convention with the phase factor $e^{i(\mathbf{K}\cdot\mathbf{r}-\omega t)}$ with the momentum transfer K from the x rays to the crystal. Since the absolute configuration of the enantiomorphic compounds was firstly determined for tartaric acid[15] using the dispersion correction, this method has developed after the advent of the synchrotron radiation source and is known as Multi-wavelength Anomalous Diffraction (MAD),[16,17] and is extensively developed to study the absolute configurations for biochemical compounds. The method requires to measure the diffraction pattern at several energies around the K or L absorption edges of the resonant scattering elements.

Our method is quite different from the above. We observe *space-group forbidden* reflections at the resonant energy in the vicinity of the absorption edge, where the scattering length is sensitive to the polarization in the primary and secondary x rays. Some *forbidden* Bragg indices turn to be *allowed*, when the equivalency of the local atomic configuration around the resonant scatterer in a unit cell is broken by the screw axis or the glide plane.

The dispersion correction terms in the vicinity of the absorption edge are written as

$$f' + if'' = m \sum_{n,g} \left(\frac{\Delta}{\hbar} \right)^2 \frac{\langle g \left| \hat{o}_s^* \right| n \rangle \langle n \left| \hat{o}_i \right| g \rangle}{\hbar\omega - \Delta + i\Gamma/2} \ , \tag{2}$$

where g and n label the ground and intermediate states, respectively. The difference energy $\Delta = \mathcal{E}_n - \mathcal{E}_g$, where $\mathcal{E}_g$ and $\mathcal{E}_n$ are their corresponding energies, and $|g\rangle$ and $|n\rangle$ are their wave functions. The electron mass is denoted by m, $\hbar\omega$ is the photon energy, Γ is a phenomenological broadening depending on the photoelectron kinetic energy and the core-hole width, and i and s label the incoming and scattered waves. The transition operator, dominated by its electric part and taken to second order, is given by

$$\hat{o} = (\boldsymbol{\epsilon} \cdot \mathbf{r}) \left\{ 1 + \frac{i}{2} (\mathbf{k} \cdot \mathbf{r}) \right\} \ , \tag{3}$$

The first term in the equation gives the electric dipole or $E1$ transition and the second one gives the electric quadrupole or $E2$ transition. The compound $DyFe_3(BO_3)_4$ belongs to one of the enantiomorphic space-group pair, $P3_121$ and $P3_221$ in the low temperature phase, where the inversion symmetry is broken, hence the $E1E2$ term in Eq. 2 is allowed for the forbidden reflections. However, the contribution is possibly negligible as is discussed later.

III. STRUCTURE OF $DyFe_3(BO_3)_4$

The compound $DyFe_3(BO_3)_4$ consists of DyO_6 trigonal prisms with a Dy^{3+} ion in the center, FeO_6 octahedra with a Fe^{3+} ion in the center, and BO_3 triangles with a B^{3+} ion in the center.[18] It belongs to trigonal space-group $R32$ (#155) at room temperature. The structure has an alternative stacking of BO_3 network planes and Dy plus Fe planes along the c axis. Space group $R32$ belongs to one of the 65 enantiomorphic space groups, and includes the right-handed screws 3_1 or left-handed screws 3_2 inside so that the crystal can have two choices for the atomic configuration. Indeed, the chain of the FeO_6 octahedra can form, in two ways, a right-handed or a left-handed screw along the c axis in $R32$. These

two atomic configurations, which are mirror images to each other, coexist in a single crystal with large chiral domains.[14]

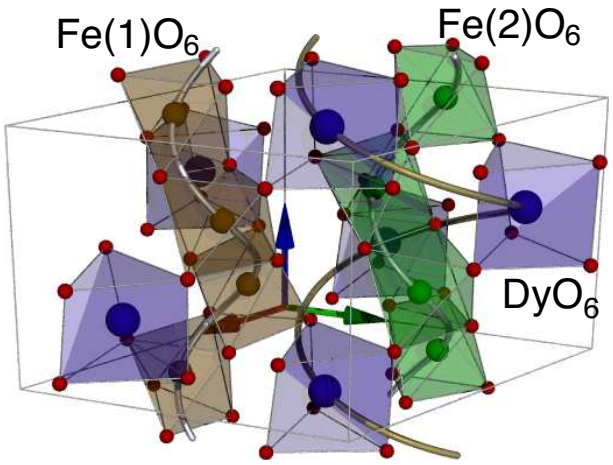

FIG. 1. A view of the atomic configuration of the *left-handed* $DyFe_3(BO_3)_4$ in space group $P3_221$ (#154). The FeO_6 octahedra and the DyO_6 trigonal prisms are colored by brown and blue, respectively. The Fe(1) ions are at the 3*a* site, and the Fe(2) are at the 6*c* site. The unit-cell is shown by gray lines. Yellow and gray helices represent spiral arrangements of Dy and Fe ions, respectively.

This compound has a first-order structural phase transition at $T_S \approx 285$ K,[19,20] where the right-handed and left-handed structure in the space group $R32$ turn into the space groups $P3_121$ (#152) and $P3_221$ (#154), respectively on decreasing temperature. In these enantiomorphic space-group pair $P3_121$ and $P3_221$, the stacking chain of the Dy^{3+} ions forms in a right-handed or a left-handed screw along the c axis, respectively. Figure 1 displays the atomic structure of the *left-handed* $DyFe_3(BO_3)_4$ in space group $P3_221$. Note that the screw chain of the Dy^{3+} ions in the low temperature phase ($T < T_S$) succeeds the handedness of the chain of Fe^{3+} ions in the high temperature $R32$ phase ($T > T_S$). In the low temperatures, this compound has an additional phase transition at $T_N = 38$ K where both of Fe and Dy magnetic moments shows an antiferromagnetic (AF) order.[19] In the AF ordered phase, $DyFe_3(BO_3)_4$ exhibits a magnetoelectric effect accompanied by a spin flop.[21]

IV. EXPERIMENTAL

The experiment was carried out at the beam line 29XUL at SPring-8 in Harima, Japan. A subsidiary experiment was carried out at the beam line 3A at PF in Tsukuba, Japan. A plate-like single crystal of $DyFe_3(BO_3)_4$ was mounted on a copper holder in a liquid He flow-type cryostat on a four-circle diffractometer. The handedness of this crystal has been found to be *left-handed*, space group $P3_221$ (#154) in the previous experiment.[14] The sample size was about 2 mm × 2 mm × 0.5 mm. The size of the incident beam was 0.5 mm×0.5 mm. A scintillation detector was used to observe the diffracted beam. The intensity of the incident beam was monitored by an ionization chamber. The incident energy was tuned by a Si (111) double-crystal-monochromator followed by a pair of Si mirrors coated by rhodium in order to cut the higher harmonic x rays at the beam line 29XUL. The helicity of the circularly polarized x-ray beam was manipulated by a diamond phase retarder with 0.6 mm in thickness. We employed the $2\overline{2}0$ reflection of the diamond of which surface is parallel to (111). In the experiment at PF, we used only a $\boldsymbol{\sigma}$ linearly polarized x-ray beam. We measured the intensity of space-group forbidden reflections 004 and 005 at two absorption edges Dy L_3 at $E = 7.796$ keV and Fe K at $E = 7.13$ keV in a temperature range from $T = 30$ K to $T = 305$ K.

Our diffraction geometry is illustrated in Fig. 2. The azimuth angle Ψ is a rotation of the sample about the scattering vector $\mathbf{K} = \mathbf{k}_i - \mathbf{k}_f$. The vectors $\mathbf{k}_i$, and $\mathbf{k}_f$ are the propagation vectors for the incident beam and the diffracted beam, respectively. We define the origin of the azimuth angle $\Psi = 0$ with respect to the direction of the reciprocal lattice vector $\mathbf{a}^*$ when it is parallel to the $-y$ axis, or $\mathbf{a}^* \| -(\mathbf{k}_i + \mathbf{k}_f)$, and the positive direction of Ψ to be the counter-clockwise rotation as viewed looking up along the scattering vector $\mathbf{K}$. The polarization of the incident x-ray beam is defined by the unit vectors $\boldsymbol{\sigma}$ and $\boldsymbol{\pi}$.

The average polarization state is expressed with the Stokes parameters P_1, P_2, and P_3 where $P_3 = +1$ and $P_3 = -1$ correspond to the linear polarization parallel to the unit vectors $\boldsymbol{\sigma}$ and $\boldsymbol{\pi}$, respectively, $P_2 = +1$ and $P_2 = -1$ correspond to the circular polarization, represented by $\frac{1}{\sqrt{2}}(\boldsymbol{\sigma} + i\boldsymbol{\pi})$ and $-\frac{1}{\sqrt{2}}(\boldsymbol{\sigma} - i\boldsymbol{\pi})$, respectively, $P_1 = +1$ and $P_1 = -1$ corresponds to the linear polarization along the diagonal directions between $\boldsymbol{\sigma}$ and $\boldsymbol{\pi}$, represented by $\frac{1}{\sqrt{2}}(\boldsymbol{\sigma} + \boldsymbol{\pi})$ and $\frac{1}{\sqrt{2}}(\boldsymbol{\sigma} - \boldsymbol{\pi})$, respectively. For the circularly polarized $P_2 = +1$ (-1) state, the $\boldsymbol{\pi}$ $(\boldsymbol{\sigma})$ component lags the $\boldsymbol{\sigma}$ $(\boldsymbol{\pi})$ by 90° according to the phase factor $\exp i(\mathbf{k} \cdot \mathbf{r} - \omega t)$.

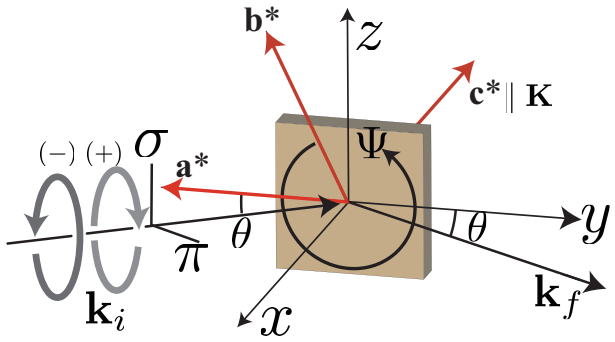

FIG. 2. (Color online) A schematic view of the diffraction geometry with a right-handed coordinates x, y, and z. The scattering vector $\mathbf{K} = \mathbf{k}_i - \mathbf{k}_f$ is antiparallel to the x axis. The marks (+) and (−) denote the positive and negative helicity of the incident beam, respectively. Here $\mathbf{k}_i$ and $\mathbf{k}_f$ are the propagation vectors of the incident and diffracted x rays, respectively, and θ denotes the Bragg angle. The $\boldsymbol{\sigma}$ and $\boldsymbol{\pi}$ components are the unit vectors which represent the polarization of the incident beam. Here the $\boldsymbol{\sigma}$ component is perpendicular to the plane of scattering, $\boldsymbol{\sigma} = (0, 0, 1)$, and the $\boldsymbol{\pi}$ component is parallel to the plane of scattering, $\boldsymbol{\pi} = (\cos\theta, \sin\theta, 0)$. For the diffracted beam, $\boldsymbol{\sigma}' = \boldsymbol{\sigma}$ and $\boldsymbol{\pi}' = (\cos\theta, -\sin\theta, 0)$.

Here unit vectors $\boldsymbol{\sigma}$, $\boldsymbol{\pi}$, and $\hat{\mathbf{k}}_i = \mathbf{k}_i/|\mathbf{k}_i|$ satisfies the right-handed rule $\boldsymbol{\sigma} \times \boldsymbol{\pi} = \hat{\mathbf{k}}_i$. The polarization of the beam from the synchrotron radiation source is usually well defined and that the relation $P_1^2 + P_2^2 + P_3^2 \cong 1$ holds.

Resonant x-ray diffraction of space group forbidden reflections depends on the geometry of the scattering system as well as the energy of the x-ray beam. This is because it depends on the polarization state of the x-ray beam as described by Eq. 3, and the unit-cell structure factor is described by a tensor of the atomic multipoles. Hence the azimuth angle Ψ scan gives important information not only about the symmetry of the local structure of the resonant ions, but also about the components of the atomic multipoles.

V. RESULTS

A. X-ray absorption spectra

The x-ray absorption spectrum (XAS) and the energy dependence of the space-group allowed reflection 003 in the vicinity of Dy L_3 and Fe K absorption edge are shown in

top panels of Figs. 3 and 4, respectively. The XAS were observed by measuring the total fluorescence yield. The maximum absorption, so called the white line, of the Dy L_3 edge and that of the Fe K edge was found at $E = 7.794$ keV and $E = 7.125$ keV, respectively while the minimum intensity of reflection 003 around the Dy L_3 edge and around the Fe K edge was found at $E = 7.788$ keV and at $E = 7.120$ keV, respectively.

We have successfully observed space-group forbidden reflections 004 and 005 in the vicinity of both absorption edges. The intensity of these forbidden reflections is about an order of 10^{-4} to that of space-group allowed reflection 003. The resonant effect for the forbidden reflections is not easily specified from the x-ray absorption spectra and the energy spectrum of reflection 003 for both absorption edges. In order to observe the underlying resonant effect precisely, we performed energy scans for forbidden reflection 004 at several azimuth angles Ψ in a small range. Bottom panels of Figs. 3 and 4 show energy spectra of the intensity of reflection 004 around the Dy L_3 and the Fe K edges, respectively. As observed, reflection 004 is accompanied by strong multiple scattering effect or *Umweganregung* effect which adds apparently random bumpy structure to the spectra, which varies with the azimuth angle as well as the x-ray energy.[22,23] The underlying resonant enhancement is present under the intensity curves of reflection 004, which are bumpy due to the multiple scattering effect. The same manner was taken for deducing the Te L_1 resonant enhancement previously.[11] The enhancement for both absorption edges, observed as a single peak around $E = 7.796$ keV for the Dy L_3 edge and three peaks around $E = 7.13$ keV for the Fe K edge, is shown by the colored areas in the bottom panels of Figs. 3 and 4, respectively. The feature of three peaks around Fe K absorption edge has been reported in the literature, for example, FeS_2.[24] We employed $E = 7.796$ keV for the Dy L_3 absorption edge and $E = 7.13$ keV for the Fe K absorption edge in the following experiments.

B. Azimuth angle scans

We have performed azimuth angle scans for forbidden reflections 004 and 005 at $E = 7.796$ keV for the Dy L_3 absorption edge and $E = 7.13$ keV for the Fe K absorption edge with the positive and negative circular polarized x-ray beam. At each fixed azimuth angle Ψ, we measured the integrated intensity by ω scan. The state of the x-ray polarization was manipulated by the diamond phase retarder for both absorption edges; the Stokes parameters

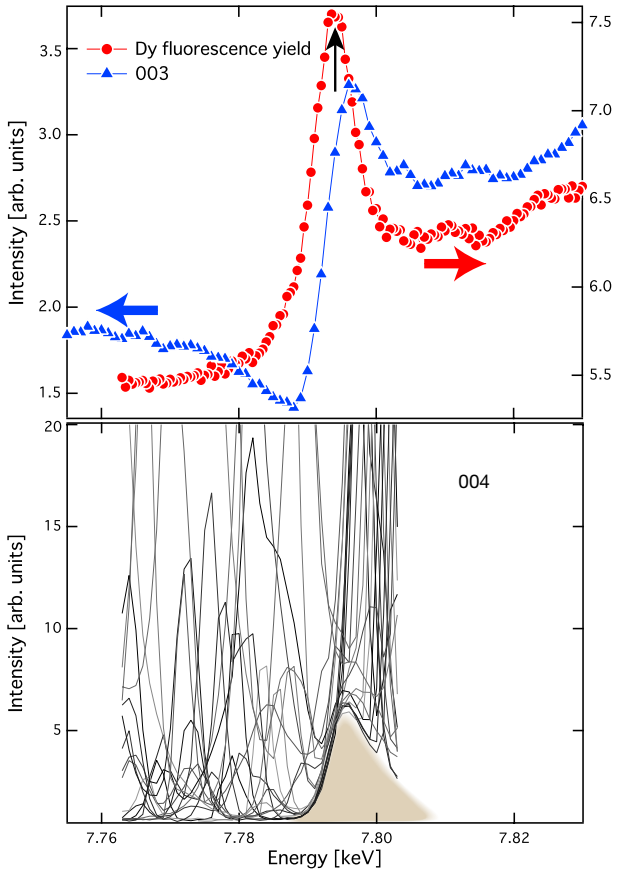

FIG. 3. (Color online) Energy spectra of the x-ray absorption, the intensity of reflection 003, and that of forbidden reflection 004 around the Dy L_3 absorption edge. The data were observed at the beam line 3A in PF with the σ polarized incident beam. Top: the x-ray absorption spectrum obtained in the total fluorescence mode is shown by red circles and the intensity of reflection 003 is shown by blue triangles. The absorption effect is not corrected. The white line (the maximum absorption) is shown by a black arrow. Bottom: the intensity of reflection 004 as a function of the x-ray energy was observed for the azimuth angle Ψ which was scanned in a range from 131.5 to 133.4° by every 0.1 degree step at $T = 200$ K. The resonant effect underlying in the intensity of reflection 004 is colored around $E = 7.796$ keV.

are summarized in Table I. The values are given from the deviation angle in θ for Bragg reflection $2\bar{2}0$ of the diamond retarder. Here (+) and (−) represent the helicity positive ($P_2 > 0$) and the helicity negative ($P_2 < 0$) states for the circularly polarized x-ray beam, respectively. Hereafter we use symbols (+) and (−) for the positive and negative x-ray helicity, respectively. Because of an accidental inaccuracy for positioning the diamond phase

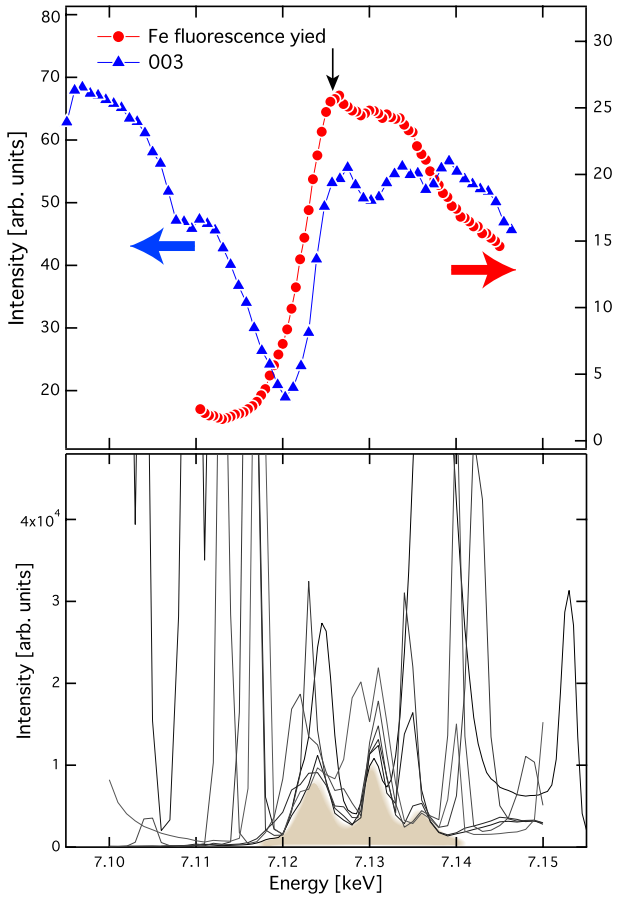

FIG. 4. (Color online) Energy spectra of the x-ray absorption, reflection 003, and forbidden reflection 004 around the Fe K absorption edge. The data were observed at the beam line 29XUL in SPring-8 with the π polarized incident beam. Top: the x-ray absorption spectrum obtained in the total fluorescence mode is shown by red circles and the intensity of reflection 003 is shown by blue triangles. The absorption effect is not corrected. The white line (the maximum absorption) is shown by a black arrow. Bottom: the intensity of reflection 004 as a function of the x-ray energy was observed for azimuth angles $\Psi = -100$, -105, -110, -114, -115, and -126° at $T = 50$ K. The resonant effect underlying in the intensity of reflection 004 is colored around $E = 7.13$ keV.

retarder, we found that the P_3, the linear polarization, had unintended non-negligible values for both the positive and the negative circularly polarized x rays, while the P_1, the diagonal linear polarization, had negligible values. Accordingly, the values of P_2 are not exactly the same for both $(+)$ and $(-)$ states, except the sign. This small deviation in P_2, however, does not matter for the following analysis for the quadrupole moment as we discuss later.

Figures 5 and 6 show the integrated intensity of reflections 004 and 005 for the $(+)$

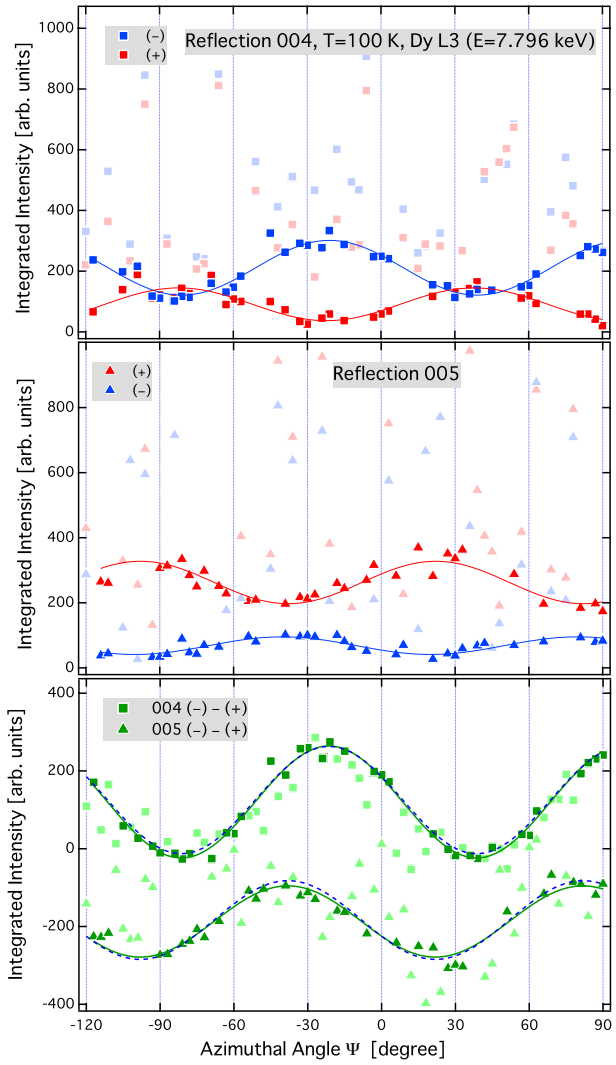

FIG. 5. (Color online) The integrated intensity of forbidden reflections 004 (top panel) and 005 (middle panel) observed by ω scan at the Dy L_3 absorption edge ($E = 7.796$ keV) and $T = 100$ K as a function of Ψ. Red squares (triangles) show the integrated intensity measured by the incident beam with the (+) helicity for reflection 004 (005) and blue squares (triangles) show that measured by the incident beam with the (−) helicity for reflection 004 (005). The bottom panel shows the difference intensity, (−) − (+), between the two helicity states. The cosine curves are results of fit to the data with Eq. 14 for the top and middle panels, and fit to the data with Eq. 18 for the bottom panel. The points colored faintly are strongly influenced by the multiple scattering effect, and are removed for the fitting. The dash lines in the bottom panel are given from the result of the least square method described in the text.

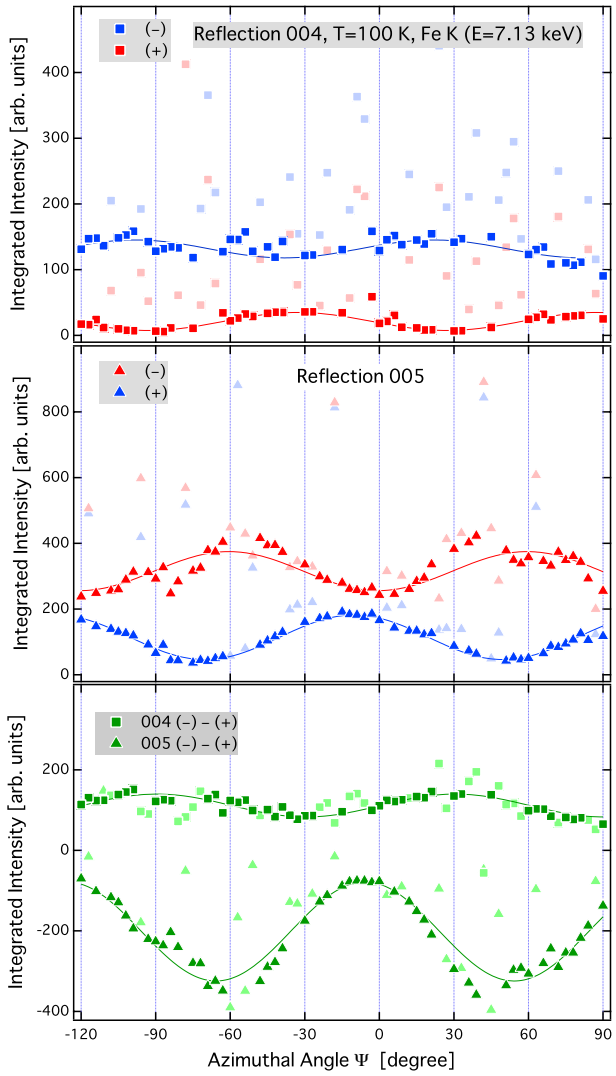

FIG. 6. (Color online) The integrated intensity of forbidden reflections 004 (top panel) and 005 (middle panel) observed by ω scan at the Fe K absorption edge ($E = 7.13$ keV) and temperature $T = 100$ K as a function of Ψ. Red squares (triangles) show the integrated intensity measured by the incident beam with the (+) helicity for reflection 004 (005) and blue squares (triangles) show that measured by the incident beam with the (−) helicity for reflection 004 (005). The bottom panel shows the difference intensity, (−) − (+), between the two helicity states. The cosine curves are results of fit to the data with Eq. 14 for the top and middle panels, and fit to the data with Eq. 18 for the bottom panel. The points colored faintly are strongly influenced by the multiple scattering effect, and are removed for the fitting.

TABLE I. The values of experimental Stokes parameters for two circularly polarized states, (+) and (−), at Dy L_3 ($E = 7.796$ keV) and Fe K ($E = 7.13$ keV) absorption edges, together with the angle of the diamond crystal, $\theta_{2\bar{2}0}$ for each polarization state.

		$\theta_{2\bar{2}0}$ (degree)	P_1	P_2	P_3
Dy L_3 7.796 keV	(+)	39.111	−0.0152	+0.978	−0.114
	(−)	39.073	+0.0139	−0.967	−0.203
Fe K 7.130 keV	(+)	43.612	−0.0195	+0.990	−0.023
	(−)	43.561	+0.0182	−0.986	−0.110

and (−) states and their difference intensity between two helicity states, (−) − (+), at Dy L_3 ($E = 7.796$ keV) absorption edge and at Fe K ($E = 7.13$ keV) absorption edge, respectively. All the data were measured at $T = 100$ K. The data are corrected with the experimental Lorentz factor. The absorption correction is not necessary because the incoming and outgoing beam have the same angle to the sample surface for both reflections. The range of azimuth angle Ψ for all scans is from $-120°$ to $90°$. The bumpy structure of azimuth scan curves is due to the multiple scattering effect as described in Sec. V A. Taking the difference between the two helicity states eliminates most of the multiple scattering effect and gives rather smooth azimuth curves for both reflections 004 and 005, and at both Dy L_3 and Fe K absorption edges. This is because the subtraction cancels out the multiple scattering effect which is only very weakly dependent on the sign of circular polarization. We find that these azimuth functions have a 120 degree periodicity according to the trigonal crystal symmetry, that the intensity for the (−) helicity is higher than that for the (+) helicity for reflection 004 for both absorption edges, that this relation is reversed for reflection 005. This fact exactly indicates that the sample used in this study belongs to the *left-handed* space group $P3_221$, as we discuss later. This handedness, of course, is in accord with that we determined with soft x-ray diffraction at Dy M_5 absorption edge.[14]

C. Temperature dependence

We observed the integrated intensity of forbidden reflection 004 observed at Dy L_3 and Fe K edges as a function of temperature. Figure 7 shows the integrated intensity of reflection 004 together with that of reflection 001 previously observed at Dy M_5 edge with a soft x-ray

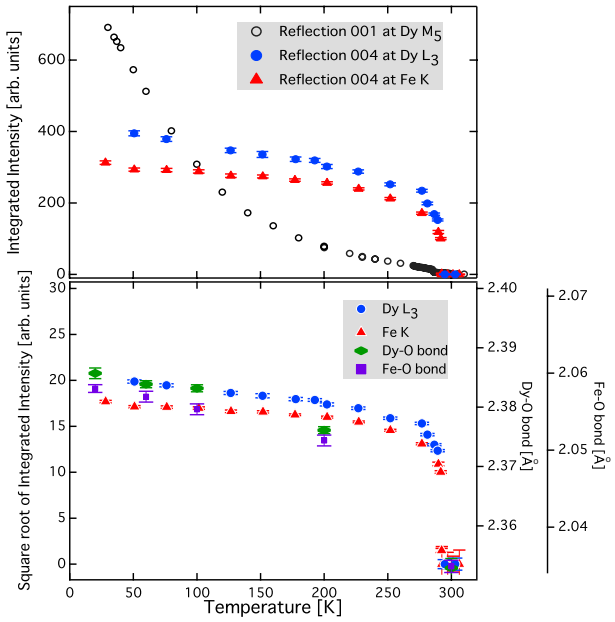

FIG. 7. (Color online) The temperature dependence of the integrated intensity of ω scans for reflection 004. Top: the integrated intensity of reflection 004 observed at Dy L_3 absorption edge (circles) and Fe K absorption edge (triangles), and that for reflection 001 observed at Dy M_5 absorption edge (open circles).[14] The integrated intensity of reflection 001 is multiplied by a factor to compare with the others. Bottom: The square root of the integrated intensity of reflection 004 observed at Dy L_3 absorption edge (circles) and Fe K absorption edge (triangles) together with the bond length of Dy-O(4) (diamonds) and the bond length of Fe(2)-O(2_1) (squares).[14]

beam.[14] We measured the intensity at several azimuth angles, where the multiple scattering effect was expected to be negligible. The data shown here is observed at one fixed azimuth angle. We find that the temperature evolution of the integrated intensities of reflection 004 observed both at Dy L_3 and Fe K edges is quite different from that of reflection 001 observed at Dy M_5 edge. They show a rather monotonous increase on cooling after the jump just below the T_S while that of reflection 001 observed at Dy M_5 edge shows a steep increase towards lower temperatures. We discuss this feature comparing with the deformation of DyO_6 trigonal prism and FeO_6 octahedron in the next Section.

VI. DISCUSSION AND ANALYSIS

A. The Dy $5d$ and Fe $4p$ quadrupole moments in the azimuth scans

The intensity I of the resonant diffraction is generally given with the Stokes parameters,[25]

$$\begin{aligned} I = & \frac{1}{2}(1+P_3)\left(|G_{\sigma'\sigma}|^2 + |G_{\pi'\sigma}|^2\right) \\ & + \frac{1}{2}(1-P_3)\left(|G_{\pi'\pi}|^2 + |G_{\sigma'\pi}|^2\right) \\ & + P_2 \mathrm{Im}\left(G^*_{\sigma'\pi}G_{\sigma'\sigma} + G^*_{\pi'\pi}G_{\pi'\sigma}\right) \\ & + P_1 \mathrm{Re}\left(G^*_{\sigma'\pi}G_{\sigma'\sigma} + G^*_{\pi'\pi}G_{\pi'\sigma}\right). \end{aligned} \tag{4}$$

Here $G_{\alpha'\beta}$ is the total resonant scattering amplitude, and α' and β are the polarization state of the diffracted and incident x-ray beam, respectively. The third term including P_2 represents the interference between σ and π components in the resonant scattering process for the circularly polarized x rays. It plays a crucial role for determination of the chirality by changing the sign coupling with the helicity of the x-ray beam.

We use the atomic multipoles, $\left\langle T^K_Q \right\rangle$, the expectation value of the spherical tensor, to express the scattering amplitude $G_{\alpha'\beta}$ as described in Ref. 25. This method is so powerful that we discuss the components of the multipole moment ordered in materials. The total scattering amplitude is composed of possible resonant events,

$$\begin{aligned} G_{\alpha'\beta} &= \sum_k r^{(k)} \frac{F^{(k)}_{\alpha'\beta}}{\hbar\omega - \Delta + \frac{i}{2}\Gamma} \\ &= \sum_k d^{(k)}(E) F^{(k)}_{\alpha'\beta}\,, \end{aligned} \tag{5}$$

where k represents individual resonant events like $E1E1$, $E1E2$ etc., Δ, Γ, and $r^{(k)}$ represent the resonant energy, its width, and the mixing parameter, respectively, and the scattering length $F_{\alpha'\beta}$ is

$$F_{\alpha'\beta} = \sum_K X^{(K)}_{\alpha'\beta} D^{(K)} \Psi^{(K)}. \tag{6}$$

Here $\Psi^{(K)}$ represents the unit-cell-structure-factor tensor of rank K which is the sum of atomic multipoles related to the resonant process, and $X^{(K)}_{\alpha'\beta}$ describes the conditions of the incident and the diffracted beam. Orientation of the crystal, with respect to states of polarization and the plane of scattering, is accomplished by a rotation matrix $D^{(K)}$. Note

that the atomic scattering length expressed by Eq. 2 is summed up in the unit-cell structure factor $\Psi^{(K)}$ including the geometric factor $X^{(K)}_{\alpha'\beta} D^{(K)}$, and that the tensorial character is emerged with the x-ray polarization.

As far as the Dy $4f$ and $5d$ quadrupole moments are concerned, the structure factor for the enantiomorphic space-group pair $P3_121$ (#152) and $P3_221$ (#154) described in Ref. 10 is applicable to $DyFe_3(BO_3)_4$ because the Dy site is at the special position $3a$ (multiplicity 3 and Wyckoff letter a), which is the same as the Si site in low-quartz. For the space groups #152 and #154, Dy ions locate at $(x,\ 0,\ \pm\frac{1}{3})$, $(0,\ x,\ \mp\frac{1}{3})$, and $(-x,\ -x,\ 0)$ in a unit cell. Here the upper and lower sign represent the space groups #152 and #154, respectively. The unit-cell structure factor is the sum of the atomic multipoles, each of which is defined at each Dy ion. First, we define the atomic multipole $\langle T^K_Q \rangle$ at the ion $(-x,\ -x,\ 0)$, which is common for both space groups, with a right-handed Cartesian axes $(\xi\eta\zeta)$. Here the ζ axis is parallel to the c-axis, and the ξ axis parallel to the [1, 1, 0] axis, which encloses an angle of 30 degrees with the reciprocal a^* axis. The atomic multipoles of the other Dy ions at $(x,\ 0,\ \pm\frac{1}{3})$, and $(0,\ x,\ \mp\frac{1}{3})$ are given as $\langle T^K_Q \rangle \exp(2\pi i Q/3)$, and $\langle T^K_Q \rangle \exp(-2\pi i Q/3)$, respectively, with a rotation along the ζ axis by $+120$, -120 degrees, respectively. The unit-cell structure factor for reflection $00l$ is

$$\begin{aligned} \Psi^K_Q = \langle T^K_Q \rangle \big\{ & 1 + \mathrm{e}^{2\pi i Q/3} \mathrm{e}^{2\pi i(\pm l/3)} \\ & + \mathrm{e}^{-2\pi i Q/3} \mathrm{e}^{2\pi i(\mp l/3)} \big\} . \end{aligned} \tag{7}$$

Here we find the selection rule for reflection $00l$ that $l + Q = 3n$ for space group $P3_121$ and $l - Q = 3n$ for space group $P3_221$, where n is an integer. The handedness emerges as the sign of Q.

The most probable resonant process at the Dy at L_3 absorption edge is the $E1E1$ event, the resonance between $2p_{\frac{3}{2}}$ and $5d$. As we discuss later, the asymmetric process $E1E2$ is negligible. The atomic multipole related to the $E1E1$ event is $\langle T^K_Q \rangle$ with rank $K = 2$, in the other words, the quadrupole. There are five independent components for the quadrupole moment with relations, $\langle T^2_{+1} \rangle' = -\langle T^2_{-1} \rangle'$, $\langle T^2_{+1} \rangle'' = \langle T^2_{-1} \rangle''$, $\langle T^2_{+2} \rangle' = \langle T^2_{-2} \rangle'$, and $\langle T^2_{+2} \rangle'' = -\langle T^2_{-2} \rangle''$. Note that the atomic multipole $\langle T^K_Q \rangle$ is a complex number defined as $\langle T^K_Q \rangle = \langle T^K_Q \rangle' + i \langle T^K_Q \rangle''$ with $\langle T^K_Q \rangle^* = (-1)^Q \langle T^K_{-Q} \rangle$. The five independent components are real numbers; $\langle T^2_0 \rangle'$, $\langle T^2_{+1} \rangle'$, $\langle T^2_{+1} \rangle''$, $\langle T^2_{+2} \rangle'$, and $\langle T^2_{+2} \rangle''$, each of which corresponds to $3\zeta^2 - r^2$, $\zeta\xi$, $\eta\zeta$, $\xi^2 - \eta^2$, and $\xi\eta$ components, respectively. Among the five components, $\langle T^2_{+1} \rangle'$, and $\langle T^2_{+2} \rangle''$ are zero for the Dy ions because the site a is on the two fold axis which

gives the relation $\langle T_Q^K \rangle = (-1)^K \langle T_{-Q}^K \rangle$. The selection rule, $l \pm Q = 3n$, for space-group forbidden reflections $00l$ ($l \neq 3n$) excludes the $\langle T_0^2 \rangle'$ component. Therefore, as far as $E1E1$ process is concerned at Dy L_3 edge, the intensity of space-group forbidden reflections is described by only two components $\langle T_{+2}^2 \rangle'$, and $\langle T_{+1}^2 \rangle''$. Note that the mirror operation between enantiomorphic space-group pair #152 and #154 gives

$$\langle T_{+1}^2 \rangle''_{\#152} = - \langle T_{+1}^2 \rangle''_{\#154} \tag{8}$$

$$\langle T_{+2}^2 \rangle'_{\#152} = \langle T_{+2}^2 \rangle'_{\#154} \ . \tag{9}$$

Eq. 9 shows that the component on the basal plane is common for both of the enantiomorphic space-group pair, while Eq. 8 shows that the component on the $\eta\zeta$ plane has the opposite sign to each other. The four amplitudes[10] for space-group forbidden reflections $00l$, $l = 3n + \mu$ ($\mu = \pm 1$) for the parity-even event $E1E1$ at Dy L_3 absorption edge are

$$G_{\sigma'\sigma} = \frac{3}{2} \langle T_{+2}^2 \rangle' \, \mathrm{e}^{i\phi_a}, \tag{10}$$

$$G_{\pi'\pi} = \frac{3}{2} \langle T_{+2}^2 \rangle' \, \mathrm{e}^{i\phi_a} \sin^2\theta, \tag{11}$$

$$G_{\pi'\sigma} = \frac{3}{2} i\lambda \left\{ \langle T_{+2}^2 \rangle' \, \mathrm{e}^{i\phi_a} \sin\theta + \langle T_{+1}^2 \rangle'' \, \mathrm{e}^{i\phi_b} \cos\theta \mathrm{e}^{3i\lambda\Psi} \right\}, \tag{12}$$

$$G_{\sigma'\pi} = \frac{3}{2} i\lambda \left\{ - \langle T_{+2}^2 \rangle' \, \mathrm{e}^{i\phi_a} \sin\theta + \langle T_{+1}^2 \rangle'' \, \mathrm{e}^{i\phi_b} \cos\theta \mathrm{e}^{3i\lambda\Psi} \right\}. \tag{13}$$

Here Bragg angle θ and the azimuth angle Ψ are shown and defined in Fig. 2. The phase factors $\mathrm{e}^{i\phi_a}$ and $e^{i\phi_b}$ emerge from Eq. 5, and depend on the x-ray energy differently to each other.[26,27] Here we introduce two parameters $\nu = \pm 1$ and $\lambda = \pm 1$. The parameter ν denotes the crystal handedness, namely $\nu = +1$ for the right-handed space group #152, and $\nu = -1$ for the left-handed space group #154, and the parameter λ denotes the product of μ and ν, $\lambda = \mu\nu$. Note that the rotating direction of Ψ is opposite to that defined in Ref. 10.

The intensity I for the $E1E1$ event at Dy L_3 absorption edge is,

$$I = I_0 + I_1 \cos 3\left(\lambda\Psi + \phi\right), \tag{14}$$

$$I_0 = \frac{1}{2} \left\{ \left(1 + \sin^2\theta\right)^2 T_a^2 + 2\cos^2\theta \, T_b^2 + P_3 \left(1 + \sin^2\theta\right) \cos^2\theta \, T_a^2 \right\} + \lambda P_2 \sin\theta \left(1 + \sin^2\theta\right) T_a^2, \tag{15}$$

$$I_1 = \left(2P_3 \sin\theta\cos\theta - \lambda P_2 \cos^3\theta\right) T_a T_b. \tag{16}$$

Here we define the parameters $\phi = \frac{1}{3}(\phi_b - \phi_a)$, $T_a = \frac{3}{2}\langle T^2_{+2}\rangle'$, $T_b = \frac{3}{2}\langle T^2_{+1}\rangle''$, and we presume $P_1 = 0$ for simplicity. Eqs. 14, 15, and 16 are the same as those of Ref. 10 in the $E1E1$ transition except the presence of the shift ϕ in Ψ. The intensity is a three-fold periodic function of the azimuthal angle Ψ. The circular polarization, P_2, is multiplied by λ, indicating that reversing the crystal chirality ν together with reversing the sign of circular polarization does not change the intensity. Only the shift ϕ in Ψ changes its sign with λ according to Eq. 14. The relation of Eq. 8 is absorbed in T_b itself in Eq. 16. By extracting it, we find

$$I_1 = \left(2\nu P_3 \sin\theta\cos\theta - \mu P_2 \cos^3\theta\right) T_a T_b, \tag{17}$$

with $T_b = T_{b(\#152)} = -T_{b(\#154)}$. Eq. 17 gives relations (i) $I_1(+\nu, \pm P_2) = -I_1(-\nu, \mp P_2)$ for the same reflection index, (ii) when $P_3 = 0$, $I_1(+\nu, \pm P_2) = I_1(-\nu, \pm P_2)$ for the same reflection index, and (iii) when $P_3 = 0$, I_1 for reflection indices $\mu = +1$ and $\mu = -1$ has the opposite sign to each other for the same values of ν and P_2. The previous observations for $DyFe_3(BO_3)_4$ and low-quartz,[9,14,26] support the relation (i), and also suggest the relation (ii) for the small value of P_3. The relation (iii) has been confirmed in the data sets of Te and $AlPO_4$.[11,12] The difference intensity between two helicity states ($P_2 = -1$ and $P_2 = +1$) is

$$I(-) - I(+) = A + B\cos 3(\lambda\Psi + \phi), \tag{18}$$

with $A = -2\lambda \sin\theta\left(1 + \sin^2\theta\right) T_a^2$, and $B = 2\mu\cos^3\theta\, T_a T_b$. Note that there are only two quadrupole components, T_a and T_b, for the intensity at Dy L_3 absorption edge.

Analyzing the Fe $4p$ quadrupole moments observed at the Fe K absorption edge is more complicated because there are nine ions in a unit cell: three of them, Fe(1) are at the special position $3a$ (multiplicity 3, Wyckoff letter a) and the other six, Fe(2) are at the general position $6c$ (multiplicity 6, Wyckoff letter c) in the low-T phase. For $00l$ reflection, six independent $4p$ quadrupole components contribute in total: they are two quadrupole components of three Fe(1) ions,

$$Q^{(1)}_{\xi^2-\eta^2} = \langle T^2_{+2}\rangle'^{(1)} e^{ip_1},$$
$$Q^{(1)}_{\eta\zeta} = \langle T^2_{+1}\rangle''^{(1)} e^{iq_1},$$

and four quadrupole components of six Fe(2) ions,

$$
\begin{aligned}
Q^{(2)}_{\xi^2-\eta^2} &= \left\langle T^2_{+2} \right\rangle'^{(2)} e^{ip_2}, \\
Q^{(2)}_{\xi\eta} &= \left\langle T^2_{+2} \right\rangle''^{(2)} e^{iq_2}, \\
Q^{(2)}_{\eta\zeta} &= \left\langle T^2_{+1} \right\rangle''^{(2)} e^{ir_2}, \\
Q^{(2)}_{\zeta\xi} &= \left\langle T^2_{+1} \right\rangle'^{(2)} e^{is_2}.
\end{aligned}
$$

The components are defined with the local coordinate $(\xi\eta\zeta)$ in the same way as Dy components. Each component is a complex number and has an independent phase factor according to Eq. 5. When $P_1 = 0$, we obtain the intensity of forbidden reflection $00l$ at Fe K edge,

$$
I = I_0 + I_1 \cos 3\left(\lambda\Psi + \phi\right) \ , \tag{19}
$$

$$
\begin{aligned}
I_0 = \frac{1}{2}\Big\{ &\left(1+\sin^2\theta\right)^2 T^2_\alpha + 2\cos^2\theta\, T^2_\beta \\
&+ P_3\left(1+\sin^2\theta\right)\cos^2\theta\, T^2_\alpha \Big\} \\
&+ \lambda P_2 \sin\theta\left(1+\sin^2\theta\right) T^2_\alpha \ ,
\end{aligned} \tag{20}
$$

$$
I_1 = \left(2\nu P_3 \sin\theta\cos\theta - \mu P_2 \cos^3\theta\right) T_\alpha T_\beta \ , \tag{21}
$$

with

$$
\begin{aligned}
T_\alpha e^{i\phi_\alpha} = 3\Big\{ &\frac{(-1)^l}{2} Q^{(1)}_{\xi^2-\eta^2} + \cos\rho\, Q^{(2)}_{\xi^2-\eta^2} \\
&- \mu\sin\rho\, Q^{(2)}_{\xi\eta} \Big\} ,
\end{aligned} \tag{22a}
$$

$$
\begin{aligned}
T_\beta e^{i\phi_\beta} = 3\Big\{ &\frac{(-1)^l}{2} Q^{(1)}_{\eta\zeta} + \cos\rho\, Q^{(2)}_{\eta\zeta} \\
&+ \mu\sin\rho\, Q^{(2)}_{\zeta\xi} \Big\} .
\end{aligned} \tag{22b}
$$

Here $\phi = \frac{1}{3}(\phi_\beta - \phi_\alpha)$ and $\rho = 2\pi l\left(\frac{1}{6} - \delta\right)$. We define δ as $0.32333 = 1/3 - \delta$, and $\delta = 0.010003$ for one of the Fe(2) ions, which is located at (0.54906, 0.335907, 0.32333) in a unit cell. Note that the parameters T_α and T_β are real numbers. As we see, Eq. 20 and Eq. 21 have the same form as Eq. 15 and Eq. 17 do, respectively, by replacing T_a and T_b with T_α and T_β. Therefore we employ the same functions to analyze the azimuth-angle-scan data sets for Dy L_3 and Fe K absorption edges.

We fit the data sets of the azimuth angle scans shown in Figs. 5 and 6 for the integrated intensity of two helicity states ($P_2 < 0$ and $P_2 > 0$) with Eq. 14, and for difference intensity, $I(-) - I(+)$ with Eq. 18, together with the origin shift ϕ in Ψ. In practice, the fitting

was carried out with selected data points to make a cosine envelop curve for each data set, otherwise, the multiple scattering prevents us from fitting properly. Some arbitrariness is inevitable for this selection, however, each curve shown in Figs. 5 and 6 traces an envelop shape in each data set very well. The results of fit are summarized in Table. II. The points colored faintly in both figures are removed for the fitting.

TABLE II: The values of the parameters as results of fit to the data sets of the azimuth angle scans for reflections 004 and 005 shown in Figs. 5 and 6. Two helicity states ($P_2 < 0$ and $P_2 > 0$) are represented by $(-)$ and $(+)$, respectively. The data sets are fit by Eqs. 14 with parameters, I_0, I_1, and ϕ, and the subtracted data, $I(-) - I(+)$, are fit by Eq. 18 with parameters, A, B, and ϕ.

		Dy L_3 edge			Fe K edge		
	Helicity (P_2)	$I_0(A)$	$I_1(B)$	ϕ	$I_0(A)$	$I_1(B)$	ϕ
004	$(-)$	211.2 ± 4.2	-90.1 ± 5.6	39.1 ± 1.3	131.3 ± 1.4	-14.7 ± 1.9	-33.7 ± 2.8
	$(+)$	90.9 ± 3.7	53.9 ± 5.0	37.8 ± 1.9	21.2 ± 0.5	13.7 ± 0.8	-32.9 ± 1.2
	$(-) - (+)$	120.3 ± 3.3	-143.9 ± 3.8	38.6 ± 0.6	109.1 ± 1.5	-26.5 ± 1.9	-33.7 ± 1.7
005	$(-)$	68.2 ± 2.3	27.1 ± 3.3	40.1 ± 2.4	114.0 ± 1.5	67.7 ± 2.2	10.2 ± 0.6
	$(+)$	262.3 ± 5.2	-65.2 ± 6.8	37.9 ± 2.2	315.4 ± 4.9	-59.4 ± 6.9	0.6 ± 2.2
	$(-) - (+)$	-187.1 ± 3.8	91.6 ± 5.0	38.1 ± 1.2	-201.4 ± 3.2	123.0 ± 5.8	5.7 ± 0.9

We find that parameter A is positive for reflection 004 and is negative for reflection 005 at Dy L_3 absorption edge, which indicates that $\nu = -1$, ie the sample we observed belongs to the left-handed space group #154. This is consistent with the previous observation at the Dy M_5 edge.[14] Likewise, the parameter A for the data observed at the Fe K edge is positive and the same discussion is applicable to the handedness of the Fe structure in this sample. Of course, the handedness of the Dy structure and the Fe structure is coincident in the same space group. Moreover, we find that the relation (iii) for I_1 in Eq. 17 is confirmed between reflections 004 and 005 at both absorption edges, and that the origin shift ϕ in Ψ is almost

unchanged for both two helicity states (−), and (+) at the Dy M_5 edge, which evidences that the $E1E1$ process is good enough to demonstrate the experimental data at the Dy L_3 edge. The discrepancy in ϕ about 12 degrees between two helicity states has been found in the study of low-quartz.[9] This discrepancy has been discussed in terms of the birefringence phenomenon, higher-order transition processes like $E1E2$, or the x-ray polarization itself.[26] Finally, it has been concluded that a tiny but non-negligible off-diagonal polarization P_1 possibly causes such discrepancy, and that the effects of higher-order transition processes and the birefringence should be very small, judging from the *ab initio* simulation and the XANES experimental data. Present data sets do not show any obvious discrepancy in ϕ between two helicity states for both reflections 004 and 005 at Dy L_3 edge. The same discussion is applicable to the origin shift ϕ in Ψ for the data observed at the Fe K edge. The values of ϕ is almost the same for both two helicity states (−), and (+) for reflection 004, although there is some deviation for reflection 005. Note that in case of Fe K edge, the origin shifts ϕ for reflection 004 and 005 is not necessarily coincident. Eq. 22 shows that six independent Fe $4p$ quadrupole components are summed up in two parameters, T_α and T_β, both of which depend on the reflection index with the interference between these sites. Consequently, the scattering amplitude does not necessarily have the same value of ϕ for reflections 004 and 005, although the circular polarization does not change ϕ.

Let us discuss about the quadrupole moments with the experimental data. Analyzing the Dy $5d$ quadrupole moments is easy because there are only two parameters, $\langle T^2_{+2}\rangle'$ and $\langle T^2_{+1}\rangle''$ in four equations. On the other hand, it is not easy for the Fe $4p$ quadrupole moments, because there are six parameters summed up in Eq. 22. We escape to deduce anything about the Fe $4p$ quadrupoles because of the complexity.

Hereafter we discuss the Dy $5d$ quadrupoles. In case of pure circularly polarized states ($P_2 = -1$ and $P_2 = +1$), Eq. 14 is applicable to solve the parameters, however, in practice, the experimental Stokes parameters described in Table I are not simple because P_3 has non-negligible values. In order to solve the parameters, we applied the least square method described in Appendix A for the equations emerged from reflections 004 and 005. The results are $\left|\langle T^2_{+2}\rangle'\right| = 7.77 \pm 0.06$ and $\left|\langle T^2_{+1}\rangle''\right| = 5.20 \pm 0.15$ for the Dy $5d$ quadrupole moment. The ratio is $r = \left|\langle T^2_{+1}\rangle''/\langle T^2_{+2}\rangle'\right| = 0.67 \pm 0.02$. The dash lines at the bottom panel of Fig. 5 reproduced with these values are quite similar to the lines obtained from the independent fits by Eq. 18. Note that the absolute values are meaningless, only the ratio has a meaning,

and that we cannot determine the signs of these components because the phase shift ϕ has arbitrariness of 60 degrees (a half period in Ψ), accompanied with the sign of I_1. The ratio $r = 0.67 \pm 0.02$ for the Dy $5d$ quadrupole moment is smaller than the ratio, $r = 1.20$, for the Dy $4f$ moment observed at $T = 100$ K,[14] in other words, the $(\eta\zeta)$ component is smaller than that of the $(\xi^2 - \eta^2)$ in Dy $5d$ moment comparing with the Dy $4f$ moment. In the following subsection, we expect that the Dy $5d$ quadrupole is strongly coupled with the deformation of DyO_6 trigonal prism as shown in Fig. 8.

B. The deformation of DyO_6 trigonal prism and FeO_6 octahedron as a function of temperature

According to the previous crystal structure analysis,[14] the structural phase transition lowers the site symmetry of Dy, which is on the three-fold rotation axis in the high-T $R32$ phase, with a translational shift along the two-fold axis and a deformation of the DyO_6 trigonal prism: the Dy-O(4) bond elongates and the Dy-O(3) and Dy-O(7) bonds shrink at $T < T_S$ while the six oxygen atoms are equidistant from the central Dy ion at $T > T_S$. Accordingly, the site symmetry of Dy changes from D_3 to C_2, losing the three-fold symmetry in the low-T $P3_121$ or $P3_221$ phase. Here the number after the chemical symbol indicates the site position in the atomic coordinate determined by the single-crystal x-ray diffraction measurements, of which information is provided in the supplementary information of Ref. 14.

Likewise, the FeO_6 octahedron deforms in the low-T phase. The Fe ions are located at site $9d$, which is at the site symmetry C_2: one of the three two-fold axes perpendicular to the c axis, in the high-T $R32$ phase. As described in the previous section, in the low-T phase, the nine Fe ions are separated into two groups: three Fe(1) ions are at the special position $3a$, remaining on one of three two-fold axes, and six Fe(2) ions are at the general position $6c$. Fig. 8 illustrates the deformation of the DyO_6 trigonal prism and $Fe(1)O_6$, $Fe(2)O_6$ octahedrons. Here pair bonds Dy-O(3), Dy-O(4), and Dy-O(7) in the DyO_6, and Fe(1)-O(1), Fe(1)-O(3), and Fe(1)-O(6) in $Fe(1)O_6$ are equidistant, respectively, in the low-T phase so as that Dy and Fe(1) ions are kept to be on the two-fold axes perpendicular to the c axis, whereas all six bonds Fe(2)-O in $Fe(2)O_6$ octahedron are different to each other.

We show the deformation of the DyO_6 trigonal prism and $Fe(1)O_6$, $Fe(2)O_6$ octahedrons as a function of temperature by taking two typical bonds, Dy-O(4) and Fe(2)-$O(2_1)$ in the

bottom panel of Fig. 7 together with the square root of the integrated intensity of reflection 004 observed at two absorption edges, Dy L_3 and Fe K. As seen, we find that the square root of the integrated intensity shows a monotonous change with temperature as well as the lengths of two bonds, Dy-O(4) and Fe(2)-O(2_1), indicating that the Dy $5d$ quadrupole moment strongly couples with ligand oxygen atoms. On the other hand, the integrated intensity of reflection 001 at Dy M_5 edge shows a drastic increase with decreasing temperature, indicating that the development of the Dy $4f$ quadrupole moment is independent of the deformation of the DyO_6 trigonal prism. This development is possibly caused by the population at the respective sub-levels in eight Kramers doublets in the ${}^6H_{\frac{15}{2}}$ state of Dy^{+3} $4f$ electrons. Note that the splitting energy between the first and the second sub-levels is estimated to be $15 \sim 20$ cm^{-1}.[20,28–30]

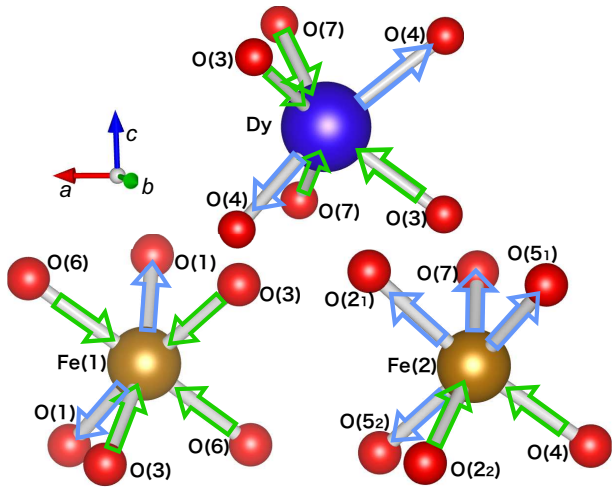

FIG. 8. (Color online) An image of deformation in a DyO_6 trigonal prism and two FeO_6 octahedra in the low-T $P3_221$ phase due to the structural phase transition at T_S. This image is drawn by VESTA.[31] Here the Fe(1) ion locates at $3a$ site and the Fe(2) ion locates at $6b$ site in the low-T $P3_221$ phase. The arrows show the direction of the elongation or the shrinkage. Pair bonds Fe(2)-O(2) lose the symmetry and that the Fe(2)-O(2_1) bond elongates and the other Fe(2)-O(2_2) bond shrinks.

VII. CONCLUSION

We have investigated the quadrupole moments of Dy $5d$ and Fe $4p$ electrons in $DyFe_3(BO_3)_4$ which has the chiral helix structure of Dy and Fe ions on the screw axes. We have per-

formed resonant x-ray diffraction with circularly polarized x-ray beam at Dy L_3 and Fe K absorption edges by swithching the sign of the x-ray helicity. The integrated intensity of forbidden reflections 004 and 005 has been observed as a function of azimuth angle Ψ and temperature.

The integrated intensity of the diffracted beam is theoretically interpreted well: (i) the periodicity of azimuth angle scan is 120 degree, which agrees with crystal symmetry, (ii) the helicity of circular polarization changes the intensity according to the crystal handedness, (iii) the phase shift ϕ in azimuthal scan is unchanged for both two helicity states $(-)$ and $(+)$ of the x-ray beam at Dy L_3 and Fe K edges, (iv) the intensity at Dy L_3 edge is described by two components of the Dy $5d$ quadrupole, (v) on the other hand, that at Fe K edge is described by totally six components of the Fe $4p$ quadrupoles for three Fe ions at the special position $3a$ and six Fe ions at the general position $6c$.

From the results (i) and (ii), we find that the crystal which we observed belongs to the left-handed space group $P3_221$, which is in accord with that we determined with soft x-ray diffraction at Dy M_5 absorption edge.[14] The result (iii) evidences that the resonant processes at both Dy L_3 and Fe K edges is well described within the scheme of $E1E1$ process, and that the birefringence phenomenon, or higher-order transition processes like $E1E2$ is unnecessary to be considered for the analysis of the experimental data. The discrepancy of the phase shift ϕ between reflections 004 and 005 observed at Fe K edge is theoretically predicted by the admixture of Fe $4p$ quadrupole moments at two sites.

From the result (iv), we have determined the ratio of two components of the Dy $5d$ moment at $T = 100$ K as $r = \left|\langle T^2_{+1}\rangle''/\langle T^2_{+2}\rangle'\right| = 0.67 \pm 0.02$, which is smaller than $r = 1.20$ for the Dy $4f$ moment.[14] The temperature dependence of the diffracted intensity shows a rather monotonous increase on cooling after the jump just below the T_S, while that of reflection 001 observed at Dy M_5 edge shows a steep increase towards lower temperatures. These results indicate that the Dy $4f$ moment is less coupled with ligand oxygen atoms than the Dy $5d$ moment.

ACKNOWLEDGMENTS

It is a pleasure to acknowledge important discussions with M. Takahashi. This work was supported by Grants-in-Aid for Scientific Research Nos. 24244058, and 25247054, MEXT,

Japan. Resonant x-ray diffraction experiments were performed at beam lines 29XUL and 17SU in SPring-8 (RIKEN Proposal Nos. 20120019, and 20130066) and beam line 3A in PF.

Appendix A: Calculation for the components of Dy $5d$ moment using the least squares method

The experimental x-ray polarization was not purely defined as $P_1 = P_3 = 0$, $P_2 = \pm 1$. We use the values of P_2 and P_3 summarized in Table I for the analysis. The value of P_1 is negligible. There are two experimental parameters, $p = \frac{9}{4}\left\langle T^2_{+2}\right\rangle'^2$, and $q = \frac{9}{4}\left\langle T^2_{+2}\right\rangle'\left\langle T^2_{+1}\right\rangle''$. The difference integrated intensity ΔI between two helicity states is

$$\begin{aligned}
\Delta I =& \Delta I_0 + \Delta I_1 \cos 3(\lambda\Psi + \phi), \\
\Delta I_0 =& I_0^- - I_0^+ \\
=& \left\{\frac{1}{2}(P_3^- - P_3^+)\cos^2\theta + \lambda(P_2^- - P_2^+)\sin\theta\right\} \\
& \times (1+\sin^2\theta)\, p, \\
\Delta I_1 =& I_1^- - I_1^+ \\
=& \left\{2(P_3^- - P_3^+)\sin\theta - \lambda(P_2^- - P_2^+)\cos^2\theta\right\} \\
& \times \cos\theta\, q.
\end{aligned} \tag{A1}$$

Here the suffixes '+' and '−' represent the positive, $P_2 > 0$, and negative, $P_2 < 0$, states, respectively. The sum of the squares of the difference between the experimental data and the theoretical functions for reflections 004 and 005 is

$$\Delta = ({}^{\rm exp}\Delta I_{004} - {}^{\rm cal}\Delta I_{004})^2 + ({}^{\rm exp}\Delta I_{005} - {}^{\rm cal}\Delta I_{004})^2. \tag{A2}$$

Here the prefixes 'exp' and 'cal' represent the experimental data set selected for the fit, and Eq. A1 including parameters p and q, respectively. The least squares method is carried out to make the sum Δ minimum. This is a simple linear-least-squares calculation, and the values of p and q are directly obtained. Finally, we find that $p = 135.7 \pm 2.14$ and $q = 90.8 \pm 2.46$, and that the components of the Dy $5d$ quadrupole are $\left|\left\langle T^2_{+1}\right\rangle\right|'' = 5.20 \pm 0.15$, $\left|\left\langle T^2_{+2}\right\rangle\right|' = 7.77 \pm 0.061$, and $r = \left|\left\langle T^2_{+1}\right\rangle''/\left\langle T^2_{+2}\right\rangle'\right| = 0.67 \pm 0.02$. Note that the sign of each

component is undetermined because the sign of I_1 depends on the arbitrariness of ϕ by 60 degrees.

---

* ytanaka@riken.jp

[1] G. H. Wagnière, *On Chirality and the Universal Asymmetry: Reflections on Image and Mirror Image* (John Wiley & Sons, 2008).

[2] L. D. Barron, Space Sci. Rev. **25**, 187 (2008).

[3] T. Kimura, Annual Review of Materials Research **37**, 387 (2007).

[4] S.-W. Cheong and M. Mostovoy, Nature Materials **6**, 13 (2007).

[5] F. Yakhou, V. Plakhty, H. Suzuki, S. Gavrilov, P. Burlet, L. Paolasini, C. Vettier, and S. Kunii, Physics Letters A **285**, 191 (2001).

[6] Y. Tanaka, U. Staub, K. Katsumata, S. W. Lovesey, J. E. Lorenzo, Y. Narumi, V. Scagnoli, S. Shimomura, Y. Tabata, Y. Onuki, Y. Kuramoto, A. Kikkawa, T. Ishikawa, and H. Kitamura, Europhys. Lett. **68**, 671 (2004).

[7] D. H. Templeton and L. K. Templeton, Acta Crystallographica Section A **36**, 237 (1980).

[8] D. H. Templeton and L. K. Templeton, Acta Crystallographica Section A **42**, 478 (1986).

[9] Y. Tanaka, T. Takeuchi, S. W. Lovesey, K. S. Knight, A. Chainani, Y. Takata, M. Oura, Y. Senba, H. Ohashi, and S. Shin, Physical Review Letters **100**, 145502 (2008).

[10] S. W. Lovesey, E. Balcar, and Y. Tanaka, Journal of Physics: Condensed Matter **20**, 272201 (2008).

[11] Y. Tanaka, S. P. Collins, S. W. Lovesey, M. Matsumami, T. Moriwaki, and S. Shin, Journal of Physics: Condensed Matter **22**, 122201 (2010).

[12] Y. Tanaka, T. Kojima, Y. Takata, A. Chainani, S. W. Lovesey, K. S. Knight, T. Takeuchi, M. Oura, Y. Senba, H. Ohashi, and S. Shin, Phys. Rev. B **81**, 144104 (2010).

[13] V. E. Dmitrienko, Acta Crystallographica Section A **39**, 29 (1983).

[14] T. Usui, Y. Tanaka, H. Nakajima, M. Taguchi, A. Chainani, M. Oura, S. Shin, N. Katayama, H. Sawa, Y. Wakabayashi, and T. Kimura, Nature Materials **13**, 611 (2014).

[15] J. M. Bijvoet, A. F. Peerdeman, and A. J. van Bommel, Nature **168**, 271 (1951).

[16] J. Karle, Int. J. Quant. Chem **7**, 357 (1980).

[17] W. Hendrickson, Trans. Am. Crystallogr. Assoc. **21**, 11 (1985).

[18] Y. Hinatsu, Y. Doi, K. Ito, M. Wakeshima, and A. Alemi, Journal of Solid State Chemistry **172**, 438 (2003).

[19] C. Ritter, A. Pankrats, I. Gudim, and A. Vorotynov, Journal of Physics: Conference Series **340**, 012065 (2012).

[20] E. A. Popova, N. Tristan, A. N. Vasiliev, V. L. Temerov, L. N. Bezmaternykh, N. Leps, B. Büchner, and R. Klingeler, The European Physical Journal B **62**, 123 (2008).

[21] Y. F. Popov, A. M. Kadomtseva, G. P. Vorob'ev, A. A. Mukhin, V. Y. Ivanov, A. M. Kuz'menko, A. S. Prokhorov, L. N. Bezmaternykh, and V. L. Temerov, JETP Letters **89**, 345 (2009).

[22] M. Renninger, Z. Kristallogr. **97**, 107 (1937).

[23] E. Weckert and K. Hümmer, Acta Crystallographica Section A **53**, 108 (1997).

[24] J. Kokubun, K. Ishida, D. Cabaret, F. Mauri, R. V. Vedrinskii, V. L. Kraizman, A. A. Novakovich, E. V. Krivitskii, and V. E. Dmitrienko, Phys. Rev. B **69**, 245103 (2004).

[25] S. W. Lovesey, E. Balcar, K. S. Knight, and J. Fernández-Rodríguez, Physics Reports **411**, 233 (2005).

[26] Y. Joly, Y. Tanaka, D. Cabaret, and S. P. Collins, Phys. Rev. B **89**, 224108 (2014).

[27] M. Takahashi, Private communication.

[28] T. Stanislavchuk, E. Chukalina, M. Popova, L. Bezmaternykh, and I. Gudim, Physics Letters A **368**, 408 (2007).

[29] D. Volkov, A. Demidov, and N. Kolmakova, Journal of Experimental and Theoretical Physics **106**, 723 (2008).

[30] A. V. Malakhovskii, A. L. Sukhachev, A. Y. Strokova, and I. A. Gudim, Phys. Rev. B **88**, 075103 (2013).

[31] K. Momma and F. Izumi, Journal of Applied Crystallography **44**, 1272 (2011).